

# On Onboard LiDAR-based Flying Object Detection

Matouš Vrba\*<sup>id</sup>, Viktor Walter\*<sup>id</sup> and Martin Saska\*<sup>id</sup>

**Abstract**—A new robust and accurate approach for the detection and localization of flying objects with the purpose of highly dynamic aerial interception and agile multi-robot interaction is presented in this paper. The approach is proposed for use onboard an autonomous aerial vehicle equipped with a 3D Light Detection and Ranging (LiDAR) sensor providing input data for the algorithm. It relies on a novel 3D occupancy voxel mapping method for the target detection and a cluster-based multiple hypothesis tracker to compensate uncertainty of the sensory data. When compared to state-of-the-art methods of onboard detection of other flying objects, the presented approach provides superior localization accuracy and robustness to different environments and appearance changes of the target, as well as a greater detection range. Furthermore, in combination with the proposed multi-target tracker, sporadic false positives are suppressed, state estimation of the target is provided and the detection latency is negligible. This makes the detector suitable for tasks of agile multi-robot interaction, such as autonomous aerial interception or formation control where precise, robust, and fast relative localization of other robots is crucial. We demonstrate the practical usability and performance of the system in simulated and real-world experiments.

## I. INTRODUCTION

With the recent rise in the popularity, availability, and utility of multirotor and fixed-wing Unmanned Aerial Vehicles (UAVs), there exists a growing concern regarding aerial safety. Reviews of recent UAV-related malpractices and accidents, such as the famous Gatwick Airport incident of 2018 when the airport was closed for three days due to a reported UAV sighting, are provided in [1], [2] and [3], which all conclude that the current aerial safety measures are insufficient to deal with unmanned vehicles. In this work, we focus on autonomous aerial interception which provides several key advantages over a manual or ground-based Counter UAV System (C-UAS). Most ground-based C-UAS rely on spoofing or jamming of the intruding UAV's navigation or radio-control signals, or on physical takedown of the UAV, which can potentially cause an uncontrolled landing or a crash of the target, endangering the people or equipment below the intruder. An Autonomous Aerial Interception System (AAIS) can capture and dispose of an intruding UAV using non-destructive means (eg. an onboard net as illustrated in Fig. 1), which is safe and the intruder can then also be used for forensics and investigation. Furthermore, because such systems can work fully or semi-autonomously, they are not prone to human error or limited by human reflexes and do not require a line of sight from a human operator to the flying target which can be obstructed by trees etc.

However, as reported in [4], the maturity of fully autonomous C-UAS' is lacking. The authors rate the maturity



Figure 1: The proposed method used during a deployment onboard an autonomous aerial interception system while eliminating an intruding DJI Mavic UAV.

of manual C-UAS systems with an Application Readiness Level (ARL) 7 out of 9, which corresponds to “functionality demonstrated”, but not proven. The maturity of autonomous C-UAS systems was rated only with an ARL 6, corresponding to “potential demonstrated”. Based on our experience with AAIS research, we conclude that this is mostly due to the lack of a suitable system for detection and localization of the target UAV [5], [6]. Such system has to be accurate, robust to false positives, various target appearances, and different environments, and provide a high update frequency with a low delay in order to enable elimination of agile maneuvering targets. To fulfill these conditions and also to ensure the security and reliability of the system, the detector should run onboard the interceptor UAV without relying on external sensors and communication. A large portion of the recent research tackling this problem was inspired by the MBZIRC 2020 international robotic competition<sup>1</sup> where one of the challenges emulated an aerial autonomous interception scenario [7], [8], [9], [10]. Complexity of the problem is well illustrated by the fact that only four teams of the 22 expert competitors were able to intercept the target even under the simplified conditions in the controlled environment of the competition. To our best knowledge, no complete and reliable solution to UAV detection and localization for autonomous aerial interception has been presented yet, and more research and development is still required.

Inspired by our solution to the MBZIRC 2020 competition which was one of the only four successful approaches and scored second place [11], we propose a new method to address the detection problem. The proposed method relies on a LiDAR sensor placed onboard the interceptor UAV and has already been employed in practice for implementation of the prototype AAIS platform Eagle.One<sup>2</sup> (pictured in Fig. 1) that is capable of autonomously eliminating a flying target. It is also suitable for general multi-robot applications where

\*Authors are with the Faculty of Electrical Engineering, Czech Technical University in Prague, Technická 2, Prague 6, matous.vrba@fel.cvut.cz.

<sup>1</sup>mrs.felk.cvut.cz/mbzirc2020

<sup>2</sup>eagle.one

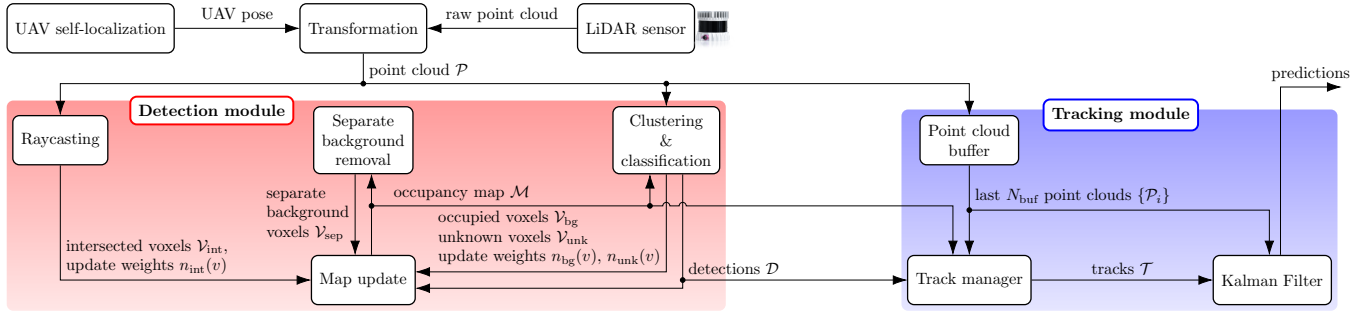


Figure 2: Overview schematic of the detection and tracking method proposed in this paper.

relative localization of the robots is required as evidenced by its deployment in a cooperative UAV navigation scenario in our previous work [12].

### A. Related works

Surveys of state-of-the-art C-UAS systems such as [1], [2] rarely consider solutions based on LiDAR detection, which are relatively sparse when compared to other detection methods such as RADAR [13], [14], visual [6], acoustic [15] or even using mixed sensors [16]. Most of the existing solutions for detecting UAVs are ground-based and rely on the assumption that the sensor is stationary, which also applies to most LiDAR-based methods such as [17] or [18]. However, these approaches are not suitable for an autonomous interception, where low delay and high accuracy positions of the target must be known, potentially over a large area. The requirement for the detector to run onboard a UAV disqualifies the methods that rely on a large or heavy sensor, such as most of the RADAR-based approaches, as well as methods assuming a static sensor or low acoustic background noise.

Visual cameras can be small and lightweight and are generally suitable for deployment onboard UAVs. There are plenty of works on UAV detection from RGB images using Convolutional Neural Networks (CNNs) or conventional computer vision methods such as [6], [19], [20], and [21]. These are useful for long-range detection of the target, but do not provide sufficiently accurate localization necessary for its physical elimination. For accurate close-range detection and localization, depth information from a stereo camera can be used either to complement an RGB detector for the localization as in [10] or to directly detect and localize the target as in [5], [22]. However, these approaches only consider a single depth or RGB image at once and do not take full advantage of the spatial information provided by the sensor over time which leads to false positives when the current scene is ambivalent. In contrast, our proposed method relies on a dynamical occupancy map of the environment that is updated using sensory data during the mission and used to detect flying objects in the area of interest. Furthermore, although our method can theoretically work with any spatial sensor, we elected to use a scanning 3D LiDAR because it has better accuracy, range, and Field of View (FoV) than comparable stereo cameras and a LiDAR can also work without external lighting and in foggy or dusty environments unlike a visual camera [23].

In aerial robotics, 3D LiDARs are used primarily for terrain and object reconstruction and Simultaneous Localization And Mapping (SLAM) (such as the LOAM-SLAM [24]), which is related to the presented study. However, SLAM algorithms typically construct only a sparse map of the features used for pose optimization in finding the current location of the robot. To detect flying objects, the algorithm presented in this work relies on a dense 3D probabilistic occupancy map of the environment.

There are several existing methods that specialize in dense occupancy mapping. A typical example is the OctoMap mapping library [25], which utilizes an OcTree [26] data structure to efficiently model the environment and raycasts the LiDAR inputs to update information about free and occupied areas in the map. Leafs of the OcTree represent explored voxels in the environment. Their associated values store information about occupancy of the voxels. The occupancy is stored in the log-odds form, which is a common approach in mapping algorithms. The value is clamped based on predefined thresholds that represent a free or occupied voxel to enable map compression. A similar approach is used in the newer UFOMap library [27], which builds upon the OctoMap by introducing new variables for each node, indicating useful information about its children and using Morton codes for more efficient traversal. A different method is presented in [28], where instead of an OcTree, a skip-list tree is used as the data structure, offering easier parallelization and faster reduction of the map to a 2.5D or 2D representation.

In contrast to common mapping approaches, the proposed detection algorithm relies on a non-compressed voxel-grid, which provides voxel lookup with an  $\mathcal{O}(1)$  asymptotic complexity and radius search with an  $\mathcal{O}(n^2)$  complexity. This enables quick updates of the map and very fast classification of the point clusters of interest, which is crucial for low-delay detection of the targets. Our algorithm also employs a more general representation of voxel occupancy supporting multi-state voxel classification and a fast reaction to dynamic obstacles. Thanks to these improvements, our detection and localization method is fast, accurate and robust using only onboard sensors of a micro-scale UAV. We present extensive experiments to evaluate the method's performance and to demonstrate its suitability for implementing an aerial interception system capable of autonomously eliminating an agile flying target. Furthermore, we provide a theoretical probabilistic analysis of the problem with applications also to general

LiDAR mapping.

## II. NOTATION

In this text, mostly a standard mathematical notation is used. In addition,  $\mathcal{M}$  is used to denote a voxel grid-map,  $v$  denotes a voxel in  $\mathcal{M}$ ,  $\mathcal{V}$  denotes a set of voxels,  $\mathcal{P}$  denotes a set of 3D points from a single scan of the LiDAR sensor (i.e. a pointcloud),  $\mathcal{C}$  denotes a cluster (subset) of points from  $\mathcal{P}$ , and  $\mathbf{p}$  denotes a point from  $\mathcal{P}$ . The number of elements in a set  $\mathcal{S}$  is denoted  $|\mathcal{S}|$ .

Furthermore, we define these relations between points and voxels as follows:  $v(\mathbf{p})$  is the voxel containing the point  $\mathbf{p}$ ,  $\mathcal{P} \cap v$  is a subset of points from  $\mathcal{P}$  contained within  $v$ , and  $\mathbf{c}_v$  is the center point of  $v$ . When referring to a distance between two voxels  $v_1$  and  $v_2$  or a voxel-point distance between  $v$  and  $\mathbf{p}$ , the Euclidean norm  $\|\mathbf{c}_{v_1} - \mathbf{c}_{v_2}\|$  or  $\|\mathbf{c}_v - \mathbf{p}\|$  is intended, respectively.

The value of a variable at a certain time-step  $t$  is indicated with a subscript  $_{[t]}$  of the variable. For brevity, time-step subscripts are omitted unless they are relevant.

## III. FLYING OBJECTS DETECTION ALGORITHM

An overview of the detection system is presented in Fig. 2. The main element of the system is a **Detection module** that relies on an occupancy voxelmap  $\mathcal{M}$ . Scans from the LiDAR are transformed to a static world frame based on the UAV's self-localization pipeline. The transformed scans  $\mathcal{P}$  are used to iteratively update  $\mathcal{M}$ . Firstly, points in  $\mathcal{P}$  are separated into euclidean clusters and classified. Voxels  $\mathcal{V}_{\text{bg}}$  containing points classified as **background** are updated with an update coefficient  $g_{\text{bg}}$  and an update weight  $n(v)$ , based on the number of points in the voxel  $v$ . Secondly, a raycasting algorithm finds the voxels  $\mathcal{V}_{\text{int}}$  intersected by the LiDAR's rays. Their corresponding update weights  $n(v)$ , which are updated using the coefficient  $g_{\text{int}}$ . In parallel, voxels  $\mathcal{V}_{\text{sep}}$  that are classified as *tentative occupied*, but are separated from *confident occupied* voxels, are detected and updated as *uncertain* in order to remove trails of occupied voxels left by dynamic obstacles. Finally, the point clusters within *uncertain* or *confident free* voxels, although surrounded by *confident free* voxels, are classified as detections of flying objects  $\mathcal{D}$  and are the output of the detector.

A **Tracking module** is used to associate subsequent detections corresponding to the same objects, to estimate and predict the targets' states, and to compensate the processing delay of the detector. It receives the point clouds  $\mathcal{P}$ , detections  $\mathcal{D}$ , and the latest occupancy map  $\mathcal{M}$ . A buffer keeps the last  $N_{\text{buf}}$  point clouds as sorted by the time of acquisition. When a new set of detections  $\mathcal{D}$  is obtained, the corresponding point cloud is selected in the buffer. Each detection is then tracked through subsequent point clouds in the buffer to the latest one using a Kalman Filter (KF)-based multi-target tracking algorithm. The multi-target tracker also uses the latest map  $\mathcal{M}$  to prevent track association to background points.

All these algorithms are implemented using the PCL [29] and Eigen [30] libraries in C++ and within the ROS framework [31] and the MRS UAV system [32]. They run in parallel

to leverage the multi-core architectures of modern CPUs. Detailed descriptions of the algorithms follow.

### A. Environment occupancy mapping and representation

Traditional mapping algorithms typically use the log-odds representation of occupancy, as introduced in [33]. Therein, each cell  $n$  in the map at time-step  $t$  stores a single value

$$L(v | z_{[1:t]}) = \log \left( \frac{p_{\text{occ}}(v | z_{[1:t]})}{1 - p_{\text{occ}}(v | z_{[1:t]})} \right), \quad (1)$$

where  $p_{\text{occ}}(v | z_{[1:t]})$  is an estimate of the probability that cell  $v$  is occupied based on the measurements  $z_{[1:t]}$ . Values of the cells are updated with each new point cloud  $\mathcal{P}$  using points  $\mathbf{p} \in \mathcal{P}$  and the LiDAR's rays. The update rule is based on the Markov assumption of time-independence and the Bayes' theorem for posterior probability,

$$p(A | B) = \frac{p(B | A)p(A)}{p(B)}. \quad (2)$$

Expanding eq. (2) for  $p_{\text{occ}}(v | z_{[1:t]})$  results in a complex expression containing several variables that are difficult to quantify in practice. Using the probability-odds representation cancels these variables out and simplifies the update rule. Assuming a prior occupancy probability  $p_{0,\text{occ}}(v) = 0.5$  and using a logarithm of the odds for numerical stability as is done in eq. (1), the update rule

$$L(v | z_{[1:t]}) = L(v | z_{[1:t-1]}) + L(v | z_{[t]}) \quad (3)$$

is obtained. This update rule is typically parametrized by two values,  $l_{\text{occ}}$  and  $l_{\text{free}}$ , as

$$L(v | z_{[t]}) = \begin{cases} l_{\text{occ}} & \text{if } v \text{ contains any point } \mathbf{p} \in \mathcal{P}, \\ l_{\text{free}} & \text{else if a ray passes through } v, \\ 0 & \text{otherwise.} \end{cases} \quad (4)$$

The state of a voxel  $v$  can be discretely classified (e.g. for planning or compression purposes) based on some predefined thresholds,  $L_{\text{occ}}$ ,  $L_{\text{free}}$ , as

$$\text{state}(v) = \begin{cases} \text{confident occupied} & \text{if } L(v) \geq L_{\text{occ}}, \\ \text{confident free} & \text{if } L(v) \leq L_{\text{free}}, \\ \text{uncertain} & \text{otherwise.} \end{cases} \quad (5)$$

To prevent windup and improve reaction time to dynamic obstacles, the value of  $L(v)$  is often saturated to a minimal and maximal value,  $L_{\text{min}}$  and  $L_{\text{max}}$ , respectively. This limits the maximum number of updates necessary to change the voxel's state.

This model is commonly employed in many mapping algorithms [25], [27], [34] and has proved to be effective for mapping static environments, as demonstrated by the many applications relying on it [35], [36], [37]. However, it does not consider dynamic objects in the environment, which is crucial for their detection. Furthermore, this model does not allow for easily increasing the uncertainty of a cell as repeated integration of the same type of measurement will always result in the cell's log-odds to eventually converge either towards a *confident occupied* or a *confident free* value. As will be shown

later in this paper, this is unsuitable for the detection of flying objects in an environment.

To address these limitations, a different voxel occupancy representation and update rule are proposed in this paper. The proposed representation allows for a more nuanced classification of the voxels in comparison to conventional mapping of static environments. Our update rule takes into account the type of points used for updating the voxels, as classified by the method described in sec. III-B. We define thresholds  $G_i$ ,  $i = 1, 2, \dots, N_{\text{states}}$  of the voxel's value  $G(v)$  corresponding to discrete classes of the voxels with increasing confidence of occupancy. The classification of a voxel  $v$  is then

$$\text{state}(v) = \begin{cases} \text{confident occupied} & \text{if } G(v) \geq G_{N_{\text{states}}}, \\ \text{state}_i, & \text{if } G(v) \in [G_i, G_{i+1}), \\ \text{confident free} & \text{if } G(v) < G_1. \end{cases} \quad (6)$$

Specifically for the case of flying object detection, we define the following voxel states and corresponding thresholds:

$$\text{state}(v) = \begin{cases} \text{confident occupied} & \text{if } G(v) \geq G_{\text{conf}}, \\ \text{tentative occupied} & \text{if } G(v) \in [G_{\text{tent}}, G_{\text{conf}}), \\ \text{uncertain} & \text{if } G(v) \in [G_{\text{unc}}, G_{\text{tent}}), \\ \text{confident free} & \text{if } G(v) < G_{\text{unc}}. \end{cases} \quad (7)$$

To update  $G(v)$  based on a new measurement  $z_{[t]}$ , an exponential filter is employed in the form

$$G(v | z_{[1:t]}) = \frac{G(v | z_{[1:t-1]}) + G(v | z_{[t]})}{2}, \quad (8)$$

where  $G(v | z_{[t]}) = g_i$ ,  $i = 1, 2, \dots, N_{\text{meas}}$  is an update coefficient selected based on the measurement  $z_{[t]}$  and the voxel  $v$ . For the flying object detection, we use

$$G(v | z_{[t]}) = \begin{cases} g_{\text{occ}} & \text{if } v \in \mathcal{V}_{\text{bg}}, \\ g_{\text{unk}} & \text{if } v \in \mathcal{V}_{\text{unk}} \cup \mathcal{V}_{\text{det}}, \\ g_{\text{free}} & \text{if } v \in \mathcal{V}_{\text{int}}, \end{cases} \quad (9)$$

where  $\mathcal{V}_{\text{bg}}$ ,  $\mathcal{V}_{\text{unk}}$ ,  $\mathcal{V}_{\text{det}}$ , and  $\mathcal{V}_{\text{int}}$  are outputs of the respective submodules (see Fig. 2) detailed below. If  $v$  contains no point and no ray,  $G(v)$  remains unchanged. It is assumed that a single voxel can only contain points of a single class (refer to sec. III-B). Note that, voxels containing points corresponding to a detected flying object are updated using  $g_{\text{unk}}$  and not  $g_{\text{free}}$ . This is to prevent biasing the map towards free voxels in the case of false-positive detections.

If  $v$  contains multiple points, the update is applied per each point within the specific voxel. Applying eq. (8)  $n$  times using the same update coefficient  $g_i$  to update a voxel  $v$  results in

$$G(v | z_{[1:t]}) = \frac{\frac{G(v | z_{[1:t-1]})}{2} + \frac{g_i}{2} \dots + \frac{g_i}{2} + \frac{g_i}{2}}{2}, \quad (10)$$

which can be rewritten as

$$G(v | z_{[1:t]}) = \frac{G(v | z_{[1:t-1]})}{2^n} + \frac{g_i}{2^n} + \frac{g_i}{2^{n-1}} + \dots + \frac{g_i}{2}. \quad (11)$$

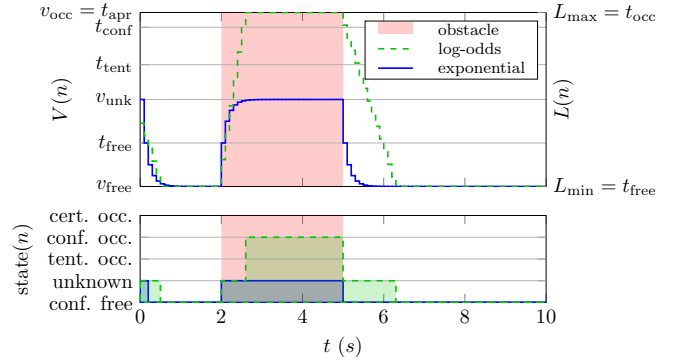


Figure 3: Comparison of  $L(v)$  and  $G(v)$  occupancy representations in a situation with a flying object entering an otherwise empty voxel at time  $t = 2$  s and leaving at  $t = 4.5$  s. Values of the parameters  $l_i$ ,  $L_i$ ,  $g_i$ ,  $G_i$  are chosen in the same way as suggested in [25] for  $L(v)$ , and the same as in the real-world experiments for  $G(v)$ . The current state according to both representations is presented in the lower graph.

The fractions of  $g_i$  can be summed as a geometric progression to obtain

$$G(v | z_{[1:t]}) = 2^{-n}G(v | z_{[1:t-1]}) + (1 - 2^{-n})g_i. \quad (12)$$

The eq. (12) allows for updating  $v$  containing multiple points in a single calculation instead of iteratively. More generally, instead of an integer number of updates, we use  $n \in \mathbb{R}$ . This can be interpreted as a weighting coefficient corresponding to the update constant  $g \in \{g_{\text{occ}}, g_{\text{unk}}, g_{\text{free}}\}$ . The calculation of  $n$  and  $g$  for a voxel  $v$  during one iteration of the detection algorithm is described in sections III-B and III-C.

The conventional log-odds voxel occupancy representation  $L(v)$  and our multi-class exponential-update representation  $G(v)$  are compared in a simulated scenario where a dynamic flying obstacle enters a voxel. Assuming that points corresponding to the obstacle are correctly identified as a **flying object**, our method never misclassifies the voxel as *confidently occupied* (unlike the log-odds representation) and reacts faster to the object leaving the voxel (see Fig. 3). These properties are crucial for the functioning of the detector to be presented further in this paper, but they can also benefit standard occupancy mapping applications.

## B. Clustering & classification

The algorithm outputs the set of occupied voxels  $\mathcal{V}_{\text{occ}}$ , their weighting coefficients  $n_{\text{occ}}(v)$ , and a set of detections  $\mathcal{D}$  for each new pointcloud  $\mathcal{P}$ . Points from  $\mathcal{P}$  are separated into clusters based on their mutual Euclidean distance using the method from [38], such that for any two clusters  $\mathcal{C}_k$ ,  $\mathcal{C}_l$ ,  $k \neq l$ , these conditions hold:

$$\mathcal{C}_k \cap \mathcal{C}_l = \emptyset, \quad (13)$$

$$\forall \{\mathbf{p}_i \in \mathcal{C}_k, \mathbf{p}_j \in \mathcal{C}_l\}, \|\mathbf{p}_i - \mathbf{p}_j\| > d_{\text{cluster}}, \quad (14)$$

and for any two points  $\mathbf{p}_i, \mathbf{p}_j \in \mathcal{C}_k$ , there exists a subset  $\{\mathbf{p}_c, \mathbf{p}_{c+1}, \dots, \mathbf{p}_{c+n}\} \subset \mathcal{C}_k$  such that

$$\begin{aligned} \|\mathbf{p}_i - \mathbf{p}_c\| &\leq d_{\text{cluster}}, \\ \|\mathbf{p}_c - \mathbf{p}_{c+1}\| &\leq d_{\text{cluster}}, \\ &\dots, \\ \|\mathbf{p}_{c+n} - \mathbf{p}_j\| &\leq d_{\text{cluster}}. \end{aligned} \quad (15)$$

Each cluster  $\mathcal{C}$  is then classified using the following rules:

- A)** If at least one point from the cluster is closer than a threshold distance  $d_{\text{close}}$  to any voxel that is at least *tentative occupied*, the cluster is classified as **background**.
- B)** If **A)** is not met and the cluster is totally separated by *confident free* voxels from any *tentative occupied* voxels, it is classified as a **flying object**.
- C)** If neither **A)** nor **B)** holds true, the cluster is classified as **unknown**.

For a single point  $\mathbf{p}$ , the condition **A)** is evaluated by iterating through all of the voxels within a cube centered on  $v(\mathbf{p})$  with edge length  $l = 2d_{\text{close}} + 1$ , checking if  $\|\mathbf{c}_v - \mathbf{p}\| < d_{\text{close}}$  and  $G(v) \geq G_{\text{conf}}$  holds for any of them. This is repeated for each point and can be trivially implemented in the voxel-grid map representation with a total computational complexity  $O(nl^2)$ .

The condition **B)** is evaluated using Algorithm 1. The algorithm is a Breadth-First Search (BFS) flood-fill approach that searches for the shortest path from a starting voxel to any *tentative occupied* voxel that is not obstructed by *confident free* voxels. If such a path is found for any  $v(\mathbf{p})$ ,  $\mathbf{p} \in \mathcal{C}$ , the algorithm terminates and **B)** is not met for  $\mathcal{C}$  (lines 15-17 of the algorithm). To prevent slowing down the algorithm when  $\mathcal{M}$  contains many *uncertain* voxels, the exploration is also terminated after reaching a border of a maximal-search cube determined by its edge length  $d_{\text{search}}$  (lines 21-23), where  $d_{\text{search}}$  is empirically determined based on the expected maximal dimensions of the targets. If the algorithm fails to find a path to either a *tentative occupied* voxel or the cube's border for any  $v(\mathbf{p})$ ,  $\mathbf{p} \in \mathcal{C}$ , all points from the cluster are enclosed by *confident free* voxels and **B)** is satisfied.

Let  $\mathcal{P}_{\text{bg}}$  be the set of all points from clusters classified as **background**,  $\mathcal{P}_{\text{det}}$  be the set of points corresponding to **flying objects**, and  $\mathcal{P}_{\text{unk}}$  be the set of **unknown** points where  $\mathcal{P}_{\text{bg}} \cap \mathcal{P}_{\text{det}} = \mathcal{P}_{\text{bg}} \cap \mathcal{P}_{\text{unk}} = \mathcal{P}_{\text{det}} \cap \mathcal{P}_{\text{unk}} = \emptyset$ . Then, the output of the clustering and classification algorithm is

$$\mathcal{V}_{\text{bg}} = \{v(\mathbf{p}) \mid \mathbf{p} \in \mathcal{P}_{\text{bg}}\}, \quad n_{\text{bg}}(v) = |\mathcal{P}_{\text{bg}} \cap v|, \quad (16)$$

$$\mathcal{V}_{\text{det}} = \{v(\mathbf{p}) \mid \mathbf{p} \in \mathcal{P}_{\text{det}}\}, \quad n_{\text{det}}(v) = \infty, \quad (17)$$

$$\mathcal{V}_{\text{unk}} = \{v(\mathbf{p}) \mid \mathbf{p} \in \mathcal{P}_{\text{unk}}\}, \quad n_{\text{unk}}(v) = |\mathcal{P}_{\text{unk}} \cap v|. \quad (18)$$

Note that,  $n_{\text{unk}}$  is infinity, so that the corresponding voxels are immediately set to the respective value. Furthermore, for each cluster  $\mathcal{C}_D$  classified as a flying object, the position  $\mathbf{r}_D$  of the detection  $D$  is calculated as

$$\mathbf{r}_D = \frac{1}{|\mathcal{C}_D|} \sum_{\mathbf{p} \in \mathcal{C}_D} \mathbf{p} = \mathbf{c}(\mathcal{C}_D), \quad (19)$$

where  $\mathbf{c}(\mathcal{C}_D)$  denotes the centroid of the cluster  $\mathcal{C}_D$ .

---

### Algorithm 1 BFS flood-fill algorithm for cluster classification.

---

```

1: Input:
2:    $\mathcal{C} = \{\mathbf{p}_1, \mathbf{p}_2 \dots \mathbf{p}_N\}$  ▷ a cluster of points
3:    $\mathcal{M}$  ▷ the current voxel-grid map
4: Output:
5:   floating  $\in \{\text{true}, \text{false}\}$  ▷ whether the cluster is surrounded by air
6: Parameters:
7:    $d_{\text{search}} \in \mathbb{N}$  ▷ the maximal search manhattan distance (in voxels)
8: for each  $\mathbf{p} \in \mathcal{C}$  do
9:    $v_0 := v(\mathbf{p})$  ▷ the starting voxel corresponding to  $\mathbf{p}$ 
10:   $\mathcal{V}_{\text{explored}} := \emptyset$  ▷ a set of voxels explored so far
11:   $\mathcal{V}_{\text{queue}} := \{v_0\}$  ▷ a FIFO queue of voxels to be explored
12:  while  $\mathcal{V}_{\text{queue}} \neq \emptyset$  do
13:     $v := \text{pop}(\mathcal{V}_{\text{queue}})$  ▷ take the first element from the queue
14:    ▷ if at least a tentative occupied voxel is reached, terminate
15:    if  $G(v) \geq G_{\text{tent}}$  then
16:      return floating := false
17:    end if
18:    ▷ if the voxel is uncertain, check it
19:    if  $G(v) \in [G_{\text{unc}}, G_{\text{tent}})$  then
20:      ▷ if a path to a border of the search cube is found, terminate
21:      if  $\|\mathbf{c}_v - \mathbf{c}_{v_0}\|_1 \geq d_{\text{search}}$  then
22:        return floating := false
23:      end if
24:      ▷ otherwise, expand the current voxel
25:      for each  $v_{\text{neigh}}$  in a 6-neighborhood of  $v$  do
26:        if  $v_{\text{neigh}} \notin \mathcal{V}_{\text{explored}} \wedge v_{\text{neigh}} \in \mathcal{M}$  then
27:          push( $v_{\text{neigh}}, \mathcal{V}_{\text{queue}}$ ) ▷ add the element to the end
28:        end if
29:      end for
30:    end if
31:    ▷ confident free voxels are not expanded
32:     $\mathcal{V}_{\text{explored}} := \mathcal{V}_{\text{explored}} \cup v$  ▷ add  $v$  to the explored set
33:  end while
34: end for
35: return floating := true ▷ if all points passed, the cluster is floating

```

---

### C. Raycasting

A generalization of the raycasting algorithm presented in [39] as three dimensions is used to find the set  $\mathcal{V}_{\text{int}}$  containing voxels intersected by the LiDAR's rays and the corresponding update weights  $n_{\text{int}}(v)$ . A set of line segments  $\mathcal{R}$  corresponding to the LiDAR's rays is obtained from the point cloud  $\mathcal{P}$ . We assume that  $\mathcal{P}$  is an *organized point cloud*, meaning that points  $\mathbf{p} \in \mathcal{P}$  are ordered in  $\mathcal{P}$  according to the corresponding physical rays of the sensor. Furthermore, an *organized point cloud* also contains points corresponding to rays that did not hit an object within the sensor's range, which are set to a reserved value  $\mathbf{p}_{\text{empty}}$ . Although these elements do not carry range information, they are important for updating empty voxels in  $\mathcal{M}$ . However, due to the nature of most LiDARs, the sensor employed in this work doesn't distinguish between ray hits below the sensor's minimal range and above the sensor's maximal range. In practice, ray hits below the minimal range correspond to the body of the UAV carrying the sensor. Thus, their order in  $\mathcal{P}$  does not change. We leverage this by manually creating a mask of element positions in  $\mathcal{P}$ , corresponding to rays that hit the body of the UAV.

Points in the point cloud  $\mathcal{P}$  are converted to line segments  $\mathcal{R}$  by iterating over  $\mathbf{p}_i \in \mathcal{P}$  and skipping over the masked-out elements. For each element  $\mathbf{p}_i$ , a line segment  $r_i$  between the

sensor's center  $\mathbf{c}_{\text{sens}}$  and an endpoint  $e_i$  is added to  $\mathcal{R}$  with

$$e_i = \begin{cases} \mathbf{c}_{\text{sens}} + d_{\text{max}} \vec{\mathbf{d}}_i, & \text{if } \mathbf{p}_i = \mathbf{p}_{\text{empty}}, \\ \mathbf{c}_{\text{sens}} + \min(d_{\text{max}}, \|\mathbf{p}_i - \mathbf{c}_{\text{sens}}\|) \vec{\mathbf{d}}_i, & \text{else,} \end{cases} \quad (20)$$

where  $\vec{\mathbf{d}}_i$  is a direction vector of the sensor's  $i$ -th ray and  $d_{\text{max}}$  is a parameter of the algorithm.

Each line segment  $r \in \mathcal{R}$  is processed by the raycasting algorithm, which provides a length  $l_{\text{int}}(v, r)$  of  $r$  within every intersected voxel  $v$ . These are accumulated for each voxel to obtain the update weights  $n_{\text{int}}(v)$ . The output of the raycasting algorithm is then

$$\mathcal{V}_{\text{int}} = \{v \mid \exists r \in \mathcal{R}, l_{\text{int}}(v, r) \neq 0\}, \quad (21)$$

$$n_{\text{int}}(v) = \sum_{r \in \mathcal{R}} l_{\text{int}}(v, r). \quad (22)$$

#### D. Separate background voxel removal

This algorithm runs in parallel to the Raycasting and Clustering & classification modules (see Fig. 2) and serves to reset the *tentative occupied* voxel clusters in  $\mathcal{M}$  that are separated from the *confident occupied* clusters. The main purpose of this algorithm is to improve the detection of a target that has taken off from the ground. In a traditional occupancy mapping method, a slow-moving object leaves a trail of occupied voxels and the points corresponding to the target are also classified as occupied (see Fig. 3). Because the mapping method presented in this paper only updates voxels as occupied if they contain points close to other occupied voxels (as explained in the previous sections), this problem is largely mitigated. However, this method can fail if an object is closer to the background than  $d_{\text{close}}$  and then leaves, such as during a UAV take-off. This module addresses this scenario, as illustrated in Fig. 4.

Firstly, voxels from  $\mathcal{M}$  with  $G(v) \geq G_{\text{tent}}$  are separated into Euclidean clusters  $\mathcal{V}_{\text{sep},i}$  using a similar method as in section III-B with a minimal inter-cluster distance  $d_{\text{sep}}$ . For each voxel cluster  $\mathcal{V}_{\text{sep},i}$ , the number of voxels that are *confident occupied* is counted:

$$n_{\text{conf},i} = |\{v \in \mathcal{V}_{\text{sep},i} \mid G(v) \geq G_{\text{conf}}\}|. \quad (23)$$

Finally, all voxels  $v \in \mathcal{V}_{\text{sep},i}$ ,  $n_{\text{conf},i} < n_{\text{conf},\text{min}}$ , where  $n_{\text{conf},\text{min}}$  is a parameter of this algorithm, are updated using the update coefficient  $g_{\text{sep}} = g_{\text{free}}$  and update weight  $n_{\text{sep}}(v) = 1$ .

#### E. A priori map initialization

In a general unknown environment, all voxels in  $\mathcal{M}$  are initialized to  $g_{\text{unk}}$ , corresponding to the *unknown* occupancy state. However, an a-priori knowledge of the environment can be utilized to initialize the map simply by setting the pre-mapped voxels to the respective values. If changing the states of the pre-mapped voxels is undesired, voxels that are known a-priori to be occupied can be set to  $\infty$  and a-priori free voxels to  $-\infty$ ; this ensures that the state of these voxels remains unchanged by the algorithms described thus far and are always classified as *confident occupied* and *confident free*, respectively.

#### F. LiDAR-based multi-target tracking

The proposed multi-target tracking algorithm is shown in Alg. 2. Input of the tracker are point clouds  $\mathcal{P}$ , detections  $\mathcal{D}$ , and occupied voxels  $\mathcal{O}$  in the map  $\mathcal{M}$ , which are all provided by the modules described above. The algorithm also relies on time-stamps  $t_{[k]}$  of the input data to accurately predict states of the tracks (see the KF model description in sec. III-F1). The tracker keeps a First In, First Out (FIFO) buffer  $\mathcal{B}$  of the latest  $N_{\text{buf}}$  point clouds ordered by their time-stamps and a set of active tracks  $\mathcal{T}$ . The algorithm is updated whenever a new point cloud is received using the `newPointCloud()` routine, and when a new set of detections is received using `newDetections()`. Both these routines rely on `updateTrack()` for state prediction, track-to-measurement association, and state correction using the associated measurement and a KF model.

1) *Track update*: The `updateTrack()` subroutine (lines 33-46 of Alg. 2) updates a track  $T$ , which consists of a state estimate  $\hat{\mathbf{x}}_T$ , its corresponding covariance matrix  $\mathbf{P}_T$ , and the number of associated detections  $n_{\text{det}}(T)$ . The state estimate

$$\hat{\mathbf{x}}_T = \begin{bmatrix} \hat{\mathbf{r}}_T^\top & \hat{\mathbf{v}}_T^\top & \hat{\mathbf{a}}_T^\top \end{bmatrix}^\top \quad (24)$$

approximates the tracked object's state vector

$$\mathbf{x} = \begin{bmatrix} \mathbf{r}^\top & \mathbf{v}^\top & \mathbf{a}^\top \end{bmatrix}^\top, \quad (25)$$

where  $\mathbf{r} \in \mathbb{R}^3$  is the position of the object,  $\mathbf{v} \in \mathbb{R}^3$  is its velocity, and  $\mathbf{a} \in \mathbb{R}^3$  is the acceleration. The covariance matrix  $\mathbf{P}_T$  represents the uncertainty of the estimate as a Gaussian distribution.  $n_{\text{det}}(T)$  can be used to reject sporadic false positives, or to select the primary track in some applications.

Firstly, development of the state and its uncertainty are predicted by  $\Delta t_{[k]} = t_{[k]} - t_{[k-1]}$  forward to the time  $t_{[k]}$  of acquisition of the input point cloud  $\mathcal{P}$ , where  $t_{[k-1]}$  is the time of the last update of  $T$ . Then, points  $\mathcal{P}'$  within the position uncertainty radius  $r_{\text{unc}}$  of the track are selected (line 36). The radius  $r_{\text{unc}} : \mathbb{R}^{3 \times 3} \rightarrow \mathbb{R}$  is a function of the track's covariance:

$$r_{\text{unc}}(\mathbf{P}_T) = \max\left(r_{\text{min}}, c_r \sqrt[3]{|\mathbf{HP}_T \mathbf{H}^\top|}\right), \quad (26)$$

where  $r_{\text{min}}$  is a minimal uncertainty radius parameter,  $c_r$  is a confidence interval for a Gaussian distribution, and  $\mathbf{H}$  is defined in eq. (30). The selected points  $\mathcal{P}'$  are separated into clusters  $\mathcal{K}$  using the same method as in sec. III-B. These clusters are filtered based on their distance to the nearest occupied voxel from  $\mathcal{O}$  (line 39) in order to remove clusters corresponding to background objects. Finally, if the filtered set  $\mathcal{K}'$  is not empty, the cluster  $\mathcal{C}$  with the centroid  $\mathbf{c}(\mathcal{C})$  closest to the track's predicted position  $\hat{\mathbf{r}}_T$  is selected. The centroid is then used as a KF measurement  $\mathbf{z}$  to correct the track's state estimate and covariance.

To update a track  $T$  using a measurement  $\mathbf{z}$  and to predict the tracked object's future trajectory, a linear KF is used. Motion of each object is modeled as a point mass with second order dynamics. Perturbances of the system are modeled as Gaussian noise. We use a standard discrete state-space mathematical representation of the model with the state vector

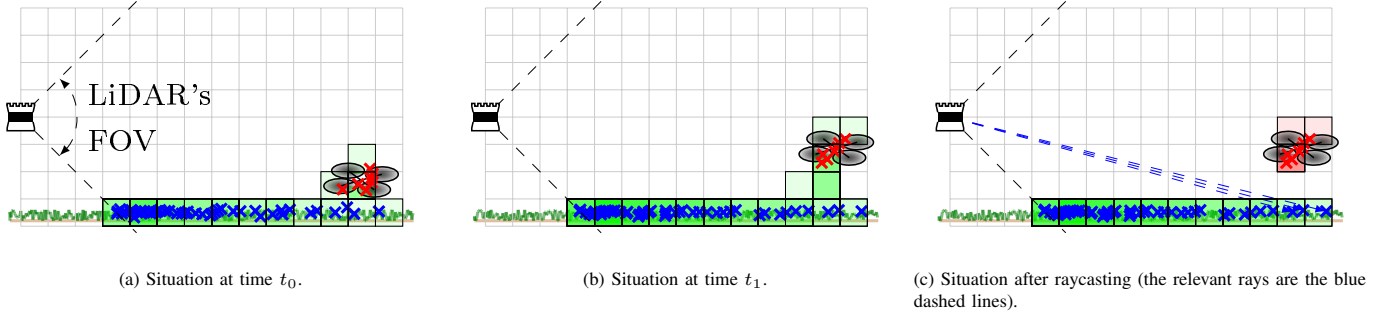


Figure 4: Illustration of a slow-moving object causing some areas of the map to be misclassified as occupied by traditional mapping algorithms. This problem can also manifest with the algorithm presented in this paper for a taking-off UAV. Points corresponding to the UAV (marked with red ‘x’ symbols) are clustered with the background points (marked blue) when it is landed (4a), marking the corresponding voxels as occupied (marked with green squares). When the UAV takes off, points of the UAV are still close to occupied voxels and the situation repeats (4b). Raycasting the new points will correctly clear out the voxels previously occupied by the UAV, but voxels currently containing points of the UAV will still be misclassified (marked red in 4c). This problem is addressed by the algorithm described in section III-D.

$\mathbf{x}$  defined above. The state-transition matrix is

$$\mathbf{A}_{[k]} = \begin{bmatrix} \mathbf{I} & \Delta t_{[k]} \mathbf{I} & \frac{1}{2} \Delta t_{[k]}^2 \mathbf{I} \\ \mathbf{0} & \mathbf{I} & \Delta t_{[k]} \mathbf{I} \\ \mathbf{0} & \mathbf{0} & \mathbf{I} \end{bmatrix}, \quad (27)$$

where  $\mathbf{I} \in \mathbb{R}^{3 \times 3}$  is an identity matrix,  $\mathbf{0} \in \mathbb{R}^{3 \times 3}$  is a zero matrix, and  $\Delta t_{[k]}$  is the duration since the previous time step  $k - 1$ . The state-space model of the track’s motion is then

$$\mathbf{x}_{[k+1]} = \mathbf{A}_{[k]} \mathbf{x}_{[k]} + \boldsymbol{\xi}_{[k]}, \quad \boldsymbol{\xi}_{[k]} \sim \mathcal{N}(\mathbf{0}, \boldsymbol{\Xi}_{[k]}), \quad (28)$$

where  $\boldsymbol{\xi}$  is Gaussian noise with zero mean and a covariance matrix  $\boldsymbol{\Xi}$ . Similarly, the measurement model is

$$\mathbf{z}_{[k]} = \mathbf{H} \mathbf{x}_{[k]} + \boldsymbol{\zeta}_{[k]}, \quad \boldsymbol{\zeta}_{[k]} \sim \mathcal{N}(\mathbf{0}, \mathbf{Z}_{[k]}). \quad (29)$$

It is assumed that the cluster centroid  $\mathbf{c}(C^*)$  used as the measurement  $\mathbf{z}$  corresponds to the position of the tracked object. The measurement matrix  $\mathbf{H}$  is therefore defined as

$$\mathbf{H} = [\mathbf{I} \quad \mathbf{0} \quad \mathbf{0}]. \quad (30)$$

The process noise covariance  $\boldsymbol{\Xi}_{[k]}$  was selected empirically parametrized as

$$\boldsymbol{\Xi}_{[k]} = \boldsymbol{\Xi} = \begin{bmatrix} \Xi_r^2 \mathbf{I} & \mathbf{0} & \mathbf{0} \\ \mathbf{0} & \Xi_v^2 \mathbf{I} & \mathbf{0} \\ \mathbf{0} & \mathbf{0} & \Xi_a^2 \mathbf{I} \end{bmatrix} \quad (31)$$

The measurement noise covariance  $\mathbf{Z}_{[k]}$  may also be selected empirically as  $\mathbf{Z}_{[k]} = \mathbf{Z} = Z^2 \mathbf{I}$  or based on known uncertainties of the sensor’s pose as discussed in sec. IV-A.

Equations (28) and (29) are used by the KF to implement the prediction and correction steps which calculate the state estimate  $\hat{\mathbf{x}}_T$  and its covariance matrix  $\mathbf{P}_T$  based on the time step  $\Delta t$  and measurement  $\mathbf{z}$  (lines 34 and 44).

2) *Point cloud update*: The newPointCloud() routine processes incoming LiDAR scans  $\mathcal{P}$ . These are used to update the buffer  $\mathcal{B}$  (lines 9-12) and the set of active tracks  $\mathcal{T}$  (lines 13-18). We assume that some tracked objects can disappear (e.g. landed or crashed UAVs) and that the detector can produce some sporadic false positives. Such objects will no longer be represented in the point clouds with non-background points and, therefore, the corresponding tracks will not be corrected

in the updateTrack() routine. The uncertainty of such tracks (represented by the covariance matrix) will grow without bounds since the KF prediction step is still applied. To filter these out, the tracks whose position uncertainty radius  $r_{\text{unc}}$  grows beyond a specified threshold  $r_{\text{max}}$  are removed from  $\mathcal{T}$ .

3) *Detections update*: Each detection  $D$  from a newly received set of detections  $\mathcal{D}$  initializes a new tentative track  $T^*$  (line 21) with a state estimate and covariance matrix

$$\hat{\mathbf{x}} := [r_D^T \quad \mathbf{0} \quad \mathbf{0}]^T, \quad (32)$$

$$\mathbf{P} := \begin{bmatrix} P_{0,r}^2 \mathbf{I} & \mathbf{0} & \mathbf{0} \\ \mathbf{0} & P_{0,v}^2 \mathbf{I} & \mathbf{0} \\ \mathbf{0} & \mathbf{0} & P_{0,a}^2 \mathbf{I} \end{bmatrix}, \quad (33)$$

where  $r_D$  is the position of the detection (obtained in eq. 19) and  $P_{0,r}$ ,  $P_{0,v}$ ,  $P_{0,a}$  are empirically determined parameters. Note that similarly as for eq. (29), the empirical initialization of the submatrix of  $\mathbf{P}$  corresponding to position can be replaced by a more accurate solution in case the pose uncertainty of the sensor is known as discussed in sec. IV-A.

This new track  $T^*$  is sequentially updated using point clouds from  $\mathcal{B}$  newer than the detection time  $t_{[k]}$  (lines 22-24). If the uncertainty of the updated track  $T^*$  is higher than  $r_{\text{max}}$ , it is considered either lost or false positive and is ignored. Otherwise, if a similar track already exists in  $\mathcal{T}$ , its number of associated detections  $n_{\text{det}}(T)$  is incremented. If  $T^*$  is valid and no similar track exists, it is added to the set of active tracks  $\mathcal{T}$  (lines 25-31). Track similarity is resolved based on the Euclidean distance of their position estimates and their uncertainty radii.

#### IV. THEORETICAL ANALYSIS

Although most 3D LiDAR mapping approaches do not consider uncertainty of the LiDAR’s position, it is seldom measured with a negligible precision in practice. This can cause inaccuracies in the resulting map if the uncertainty is not accounted for by the mapping algorithm, which may in turn then lead to false positives when such a map is used for the flying object detection as described above. To tackle this problem, we present a theoretical analysis of the probability that a ray of the LiDAR hit an object that lies within the

---

**Algorithm 2** Point cloud multi-target tracking algorithm
 

---

```

1: Input:
2:  $\mathcal{P}_{[k]} = \{\mathbf{p}\}$   $\triangleright$  a scan from the LiDAR at time-step  $k$ 
3:  $\mathcal{D}_{[k]} = \{D\}$   $\triangleright$  a set of detections at time-step  $k$ 
4:  $\mathcal{O} = \{\mathbf{c}(v) \mid v \in \mathcal{M}, G(v) \geq G_{\text{tent}}\}$   $\triangleright$  occupied voxels' centers
5:  $t_{[k]} \in \mathbb{R}$   $\triangleright$  time of time-step  $k$ 
6: Persistent state:
7:  $\mathcal{T} = \{T\}$   $\triangleright$  set of active tracks where  $T \equiv \{\hat{\mathbf{x}}_T, \mathbf{P}_T\}$ 
8: Routine newPointCloud( $\mathcal{P}_{[k]}, \mathcal{O}$ ):
9:   push( $\mathcal{P}_{[k]}, \mathcal{B}$ )  $\triangleright$  add  $\mathcal{P}_{[k]}$  to the front of the buffer
10:  if  $|\mathcal{B}| > N_{\text{buf}}$  then
11:    pop( $\mathcal{B}$ )  $\triangleright$  if the buffer is full, remove the last element
12:  end if
13:  for each  $T \in \mathcal{T}$  do
14:     $T := \text{updateTrack}(T, \mathcal{P}_{[k]}, \mathcal{O}, t_{[k]} - t_{[k-1]})$ 
15:    if  $r_{\text{unc}}(\mathbf{P}_T) > r_{\text{max}}$  then
16:       $\mathcal{T} := \mathcal{T} \setminus T$   $\triangleright$  remove too uncertain tracks
17:    end if
18:  end for
19: Routine newDetections( $\mathcal{D}_{[k]}, \mathcal{O}$ ):
20:  for each  $D \in \mathcal{D}_{[k]}$  do
21:     $T^* := \text{initializeTrack}(D)$ 
22:    for each  $\mathcal{P}_{[i]} \in \mathcal{B}, t_{[i]} > t_{[k]}$  do
23:       $T^* := \text{updateTrack}(T^*, \mathcal{P}_{[i]}, \mathcal{O}, t_{[i]} - t_{[i-1]})$ 
24:    end for
25:    if  $r_{\text{unc}}(\mathbf{P}_{T^*}) \leq r_{\text{max}}$  then
26:      if  $\forall T \in \mathcal{T}, \|\hat{\mathbf{r}}_T - \hat{\mathbf{r}}_{T^*}\| \leq r_{\text{unc}}(\mathbf{P}_T) + r_{\text{unc}}(\mathbf{P}_{T^*})$  then
27:         $n_{\text{det}}(T) := n_{\text{det}}(T) + 1$ 
28:      else
29:         $\mathcal{T} := \mathcal{T} \cup T^*$ 
30:      end if
31:    end if
32:  end for
33: Routine updateTrack( $T, \mathcal{P}, \mathcal{O}, \Delta t$ ):
34:   $T := \text{predictKF}(T, \Delta t)$ 
35:   $\triangleright$  select points within  $r_{\text{unc}}$  of the position estimate  $\hat{\mathbf{r}}_T$ 
36:   $\mathcal{P}' := \{\mathbf{p} \mid \mathbf{p} \in \mathcal{P} \wedge \|\mathbf{p} - \hat{\mathbf{r}}_T\| \leq r_{\text{unc}}(\mathbf{P}_T)\}$ 
37:   $\mathcal{K} := \text{extractClusters}(\mathcal{P}')$ 
38:   $\triangleright$  filter out clusters too close to occupied voxels  $\mathcal{O}$ 
39:   $\mathcal{K}' := \{\mathcal{C} \mid \min_{\mathbf{c}(v) \in \mathcal{O}} (\|\mathbf{c}(C) - \mathbf{c}(v)\|) > d_{\text{min}}\}$ 
40:  if  $\mathcal{K}' \neq \emptyset$  then
41:     $\triangleright$  use the centroid of the closest cluster for KF correction
42:     $\mathcal{C}^* := \text{argmin}_{\mathcal{C} \in \mathcal{K}'} \|\mathbf{c}(C) - \hat{\mathbf{r}}_T\|$ 
43:     $\mathbf{z} := \mathbf{c}(\mathcal{C}^*)$ 
44:     $T := \text{correctKF}(T, \mathbf{z})$ 
45:  end if
46:  return  $T$ 

```

---

voxel that is obtained based on the (noisy) measured pose of the sensor and the measured range.

#### A. LiDAR measurement uncertainty

Let us consider a single point corresponding to one ray of a LiDAR sensor with a known pose in a static world frame  $\mathcal{W}$ . Assuming the ground-truth of the sensor's pose and of the range measurement are known (there is no noise burdening them), the ground-truth point  $\mathbf{p}$  can be expressed in the world frame as

$$\mathbf{p} = l_{gt} \mathbf{R}_{gt} \vec{\mathbf{d}} + \mathbf{t}_{gt}. \quad (34)$$

where  $\mathbf{t}_{gt}$  and  $\mathbf{R}_{gt}$  are the position and orientation of the sensor in  $\mathcal{W}$ ,  $l_{gt}$  is the range of the ray, and  $\vec{\mathbf{d}}$  is the (unit) direction vector of the ray in the sensor frame.

A more realistic model has to include also the uncertainties of these variables. For this purpose, let us define a noise vector

$\mathbf{w}$  containing the position, orientation, and range noise, which is assumed to have a multivariate Gaussian distribution as

$$\mathbf{w} = [\mathbf{t}_n \quad \alpha_n \quad \beta_n \quad \gamma_n \quad l_n]^\top, \quad (35)$$

$$\mathbf{w} \sim \mathcal{N}(\mathbf{0}, \boldsymbol{\Sigma}_{\mathbf{w}}), \quad (36)$$

where  $\boldsymbol{\Sigma}_{\mathbf{w}}$  is the corresponding covariance matrix. The measured (noisy) pose of the LiDAR sensor and the ray length can be expressed as

$$\mathbf{t}_m = \mathbf{t}_{gt} + \mathbf{t}_n, \quad (37)$$

$$\begin{aligned} \mathbf{R}_m &= \mathbf{R}_{zm} \mathbf{R}_{ym} \mathbf{R}_{xm} \\ &= \mathbf{R}_z(\gamma_{gt} + \gamma_n) \mathbf{R}_y(\beta_{gt} + \beta_n) \mathbf{R}_x(\alpha_{gt} + \alpha_n), \end{aligned} \quad (38)$$

$$l_m = l_{gt} + l_n. \quad (39)$$

Note that to express the orientation noise, we consider a decomposition of the rotation matrix  $\mathbf{R}_{gt}$  to separate (intrinsic) rotations around the three axes  $x$ ,  $y$ , and  $z$ , because this is a common representation of orientation uncertainty used e.g. by ROS and MAVLink, but a similar approach as described in this section can be used analogously for other representations.

The measured (noisy) point  $\mathbf{p}_m$  is a realization of a random variable  $\mathbf{P}_m(\mathbf{w})$  which is obtained by substituting  $\mathbf{t}_m$ ,  $\mathbf{R}_m$ , and  $l_m$  for their ground-truth counterparts in eq. (34):

$$\mathbf{p}_m = \mathbf{P}_m(\mathbf{w}) = l_m \mathbf{R}_m \vec{\mathbf{d}} + \mathbf{t}_m. \quad (40)$$

The probability distribution of  $\mathbf{P}_m$  can be approximated using linearization as a Gaussian with a mean  $\boldsymbol{\mu}$  and a covariance matrix  $\boldsymbol{\Sigma}$ . The transformation of a known covariance  $\boldsymbol{\Sigma}_{\mathbf{w}}$  of the random variable  $\mathbf{w}$  to the covariance  $\boldsymbol{\Sigma}$  may be derived from eq. (40) as

$$\boldsymbol{\Sigma} = \mathbf{J} \boldsymbol{\Sigma}_{\mathbf{w}} \mathbf{J}^\top, \quad \mathbf{J} = \frac{\partial \mathbf{P}_m(\mathbf{w})}{\partial \mathbf{w}}, \quad (41)$$

where the Jacobian  $\mathbf{J}$  is equal to

$$\mathbf{J} = \begin{bmatrix} \mathbf{I} & l_m \mathbf{R}_{zy} \frac{\partial \mathbf{R}_x}{\partial \alpha_n} \vec{\mathbf{d}} & l_m \mathbf{R}_{zm} \frac{\partial \mathbf{R}_y}{\partial \beta_n} \mathbf{R}_{xm} \vec{\mathbf{d}} & l_m \frac{\partial \mathbf{R}_z}{\partial \gamma_n} \mathbf{R}_{yx} \vec{\mathbf{d}} & \mathbf{R}_m \vec{\mathbf{d}} \end{bmatrix}, \quad (42)$$

where  $\mathbf{R}_{zy} = \mathbf{R}_{zm} \mathbf{R}_{ym}$  and  $\mathbf{R}_{yx} = \mathbf{R}_{ym} \mathbf{R}_{xm}$ . The mean  $\boldsymbol{\mu}$  is the expected value of  $\mathbf{P}_m$ , which is obtained from eq. (40) as

$$\boldsymbol{\mu} = \mathbb{E}[\mathbf{P}_m(\mathbf{w})] = \mathbf{P}_m(\mathbf{w} = \mathbf{0}) = \mathbf{p}_m. \quad (43)$$

The approximated probability density function of  $\mathbf{P}_m$  is then

$$f_{\mathbf{P}_m}(\mathbf{p}) \approx f_{\mathcal{N}}(\mathbf{p}, \boldsymbol{\mu}, \boldsymbol{\Sigma}), \quad (44)$$

which is a multivariate normal probability density function with mean  $\boldsymbol{\mu}$  and covariance  $\boldsymbol{\Sigma}$ .

#### B. Evaluation of voxel hit probability

Let us evaluate the probability that the correct voxel is updated by a measured point  $\mathbf{p}_m$ , which may be formalized as

$$p_{\text{hit}} = p(v_m = v_{gt}) = p(\mathbf{p} \in v_m \mid \mathbf{p}_m, \boldsymbol{\Sigma}), \quad (45)$$

where  $v_m$  is the measured voxel  $v_m = v(\mathbf{p}_m)$  and  $v_{gt}$  is the ground-truth voxel actually containing the object  $v_{gt} = v(\mathbf{p})$ . It is assumed that the map is aligned with the world frame so



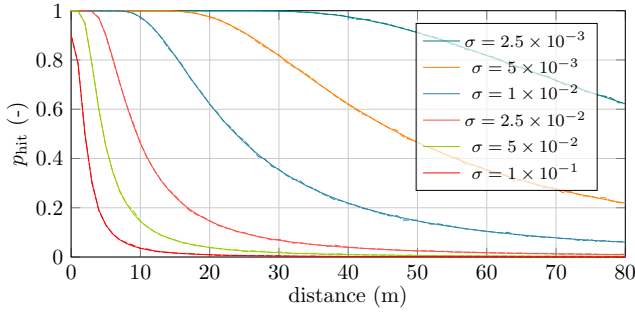


Figure 5: Probability that the voxel corresponding to a point measured by a LiDAR was really hit as a function of distance for different noise parameters  $\sigma$ .

that voxels in the map correspond to axis-aligned cubes in  $\mathcal{W}$ . The hit probability  $p_{\text{hit}}$  can be quantified as

$$p_{\text{hit}} = \int_{v_m} f_{\mathcal{N}}(\mathbf{x}, \boldsymbol{\mu}, \boldsymbol{\Sigma}) d\mathbf{x}, \quad (46)$$

where the voxel  $v_m$  in the integration limits is interpreted as the corresponding axis-aligned cube and  $f_{\mathcal{N}}(\mathbf{x}, \boldsymbol{\mu}, \boldsymbol{\Sigma})$  is the value of the multivariate normal probability density function with mean  $\boldsymbol{\mu}$  and covariance  $\boldsymbol{\Sigma}$  at point  $\mathbf{x}$ . This integral does not have an analytical solution, but effective algorithms for its numerical calculation exist [40].

### C. Target detection probability over distance

If we assume a full and correct occupancy map of the environment, a target situated within the mapped environment, and an ideal reflectivity of the target and sensitivity of the sensor, the target must be hit with at least one ray of the LiDAR to be detected by the presented method. Because the LiDAR has a limited resolution and FoV, the detection probability then depends on the sensor's parameters, and the target's shape and distance from the sensor. Given no prior information about the target's position  $\mathbf{r}$  except for its distance relative to the sensor  $l$ , let us model its position as uniformly distributed on the surface of a sphere  $S$  with radius  $l$  centered on the sensor:

$$\mathbf{r} \in S, \quad f_{\mathbf{r}}(\mathbf{r}) = \frac{1}{A_S} = \frac{1}{4\pi l^2}, \quad (47)$$

where  $f_{\mathbf{r}}(\mathbf{r})$  is a probability density function of  $\mathbf{r}$  and  $A_S$  is the surface area of  $S$ . Furthermore, let us denote the intersection point of a ray  $r$  and the sphere  $S$  as  $\mathbf{p}_{r,S}$ , the projection of the target's shape centered on  $\mathbf{p}_{r,S}$  onto the sphere  $S$  as  $P_r$ , the area of  $P_r$  as  $A_{P_r}$ , and the point reflection of  $P_r$  w.r.t.  $\mathbf{p}_{r,S}$  as  $P'_r$ .

For a single ray  $r$  of the LiDAR, the center of the target  $\mathbf{r}$  must lie within  $P'_r$  in order to be intersected by the ray. The probability of the target being intersected by  $r$  is thus

$$p_{\text{int},r} = p(\mathbf{r} \in P'_r) = \int_{P'_r} f_{\mathbf{r}}(\mathbf{r}) d\mathbf{r} = \frac{A_{P'_r}}{A_S} = \frac{A_{P_r}}{4\pi l^2}, \quad (48)$$

where  $A_{P'_r} = A_{P_r}$  is the area of  $P'_r$ . Similarly, the probability that the target is intersected at least by one ray  $r \in \mathcal{R}$  of the LiDAR is

$$p_{\text{int},\mathcal{R}} = \int_{P'_{\mathcal{R}}} f_{\mathbf{r}}(\mathbf{r}) d\mathbf{r}, \quad (49)$$

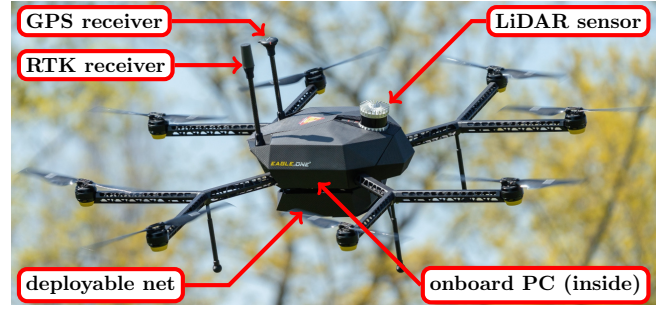


Figure 6: A schematic of the autonomous aerial interception platform EagleOne Mk4 used in the experimental evaluation.

model	horiz. rays	vertical rays	vertical FOV	scan rate	max. range	precision
OS0-128	1024	128	$\pm 45^\circ$	10 Hz	50 m	$\pm 5$ cm
OS1-128	1024	128	$\pm 22.5^\circ$	10 Hz	100 m	$\pm 5$ cm

Table I: Parameters of the sensors used in the experiments according to the manufacturer. Both sensors are Revision C.

where  $P'_{\mathcal{R}} = \{\mathbf{r} \in S \mid \exists P'_r, \mathbf{r} \in P'_r\}$  is the union of  $P'_r$  for all rays  $r \in \mathcal{R}$ .

Solving eq. (49) analytically for an arbitrary shape of the target is unfeasible, but we can approximate the target's shape as a sphere. The area  $A_{P_r}$  is then constant for all  $r$  and thus we can substitute  $A_P \equiv A_{P_r}$ .

## V. EXPERIMENTAL EVALUATION

To demonstrate performance of the presented algorithms under realistic conditions, several real-world and simulated experiments were performed. In both cases, the EagleOne Mk4<sup>3</sup> UAV platform was used, which was developed as a prototype for autonomous aerial interception. It is an octocopter frame equipped with an Ouster LiDAR sensor (see Table I), an accurate RTK-GPS, a PixHawk flight control unit including an Inertial Measurement Unit (IMU), and an Intel NUC computer [41] (see Fig. 6). The onboard computer runs the MRS UAV system [32] for self-localization, trajectory tracking and stabilization. The target UAV was a Tarot T650 frame with an approximate diameter between rotors of 0.65 m. Parameter values of the algorithms during the experiments are listed in Table II.

<sup>3</sup>eagle.one

occupancy mapping						
$v_s$	$g_{\text{occ}}$	$g_{\text{unk}}$	$g_{\text{free}}$	$G_{\text{conf}}$	$G_{\text{tent}}$	$G_{\text{unc}}$
0.25 m	0	-740	-1000	-0.1	-300	-750
clustering, raycasting and separate voxel removal						
$d_{\text{cluster}}$	$d_{\text{close}}$	$d_{\text{search}}$	$d_{\text{max}}$	$n_{\text{conf},\text{min}}$		
0.25 m	0.7 m	3 m	20 m	24		
multi-target tracking						
$N_{\text{buf}}$	$c_r$	$r_{\text{min}}$	$r_{\text{max}}$	$n_{\text{conf},\text{min}}$	$Z$	
10	0.5	1.5 m	3 m	24	1 m	
$\Xi_r$	$\Xi_v$	$\Xi_a$	$P_{0,r}$	$P_{0,v}$	$P_{0,a}$	
0.5 m	0.5 m s <sup>-1</sup>	0.1 m s <sup>-2</sup>	0.5 m	3 m s <sup>-1</sup>	3 m s <sup>-2</sup>	

Table II: Parameter values of the presented algorithms used in the experiments (see sec. III).

### A. Simulated experiments

To establish a baseline of the algorithms' performance under ideal conditions, a simulation was performed with no noise burdening the observer's selflocalization and the LiDAR sensing. The observer was equipped with a simulated LiDAR with the same ray layout and density as the Ouster OS1-128 sensor. Both the target and the observer followed various trajectories with differing mutual distance, velocities, and accelerations. The simulations were executed in the realistic Gazebo simulator<sup>4</sup> to ensure high fidelity of the simulation. The environment where the real-world experiments took place was mapped using a 3D scanner and imported into the simulator. Results from the simulations are presented in the graphs in Fig. 7 and in Table III.

It may be observed that the multi-target tracking significantly improves recall at a small cost in position accuracy. The recall is improved because tracking is preserved even in situations when detections are temporarily unavailable. In such situations, the target's predicted position may be less accurate because the KF does not receive corrections from the detections, which also causes the increased error at large distances where detection recall is lower as seen in Fig. 7c. The larger tracking error may also partially be caused by a mismatch of the KF's measurement model because it assumes noisy data. It may also be observed that with ideal data, there is no clear correlation between the observers or the targets speed or their mutual distance.

Even though all sensors in this experiment were ideal, there is an error in the detected position of the target. This error is caused by a biased sampling of the target's shape by the observer's LiDAR sensor, which is always observed only from one side during a single detection. Therefore, points from the observed side of the target are overrepresented in a single LiDAR scan and the resulting position estimate which is obtained as their mean is biased. The value of this bias depends on the target's shape, but it is always in the range  $[0, a]$ , where  $a$  is a radius of its circumscribed sphere. This corresponds well with the experimental results where a target with  $a = 0.325$  m was used.

### B. Real-world experiments

Three outdoor experiments with one target UAV and one observer UAV were executed to test the detection system under realistic conditions close to the intended deployment. Both the target and the observer were equipped with RTK-GPS which was used as a ground-truth and the observer carried the Ouster OS0-128 sensor. The first experiment consisted of manually controlled flight of both UAVs with varying speeds and mutual distance. In the second experiment, the observer autonomously followed the target based on data from the detection system, and in the third experiment, autonomous interception of the target was performed with the detector employed as a source of data for an interception planning algorithm. Results from the simulations are presented in the graphs in Fig. 8 and in Table III. It may be observed that with noise, filtering improves the average position estimation error.

<sup>4</sup>gazebo.org

	mean position error	std. dev. of pos. error
simulation	0.17 m (0.24 m)	0.10 m (0.24 m)
real-world	0.92 m (0.91 m)	0.98 m (0.76 m)

Table III: Results of the simulated and real-world experiments (values in parentheses are with multi-target-tracking).

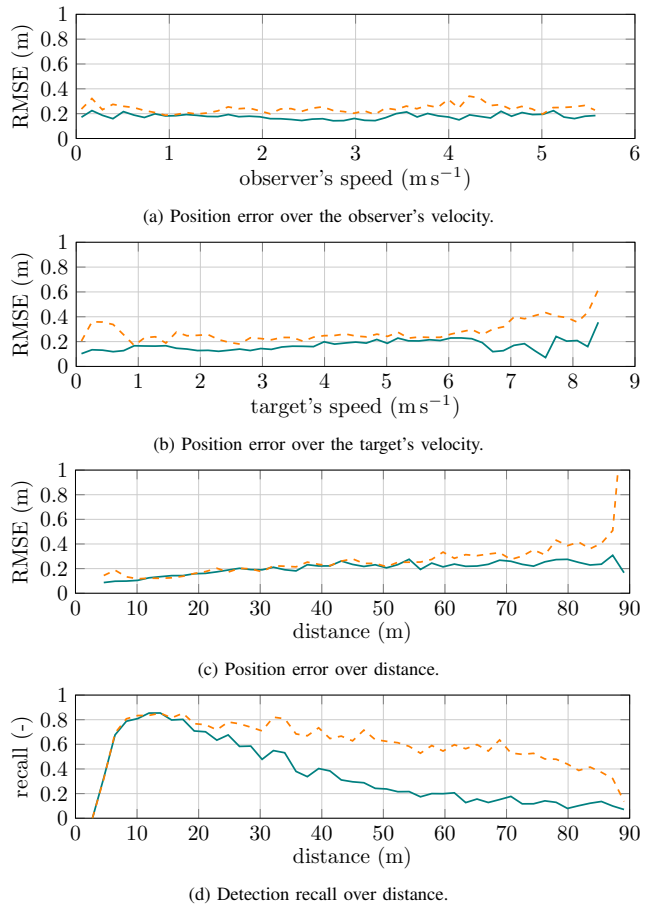


Figure 7: Results from the simulated experiments. Detected positions are in blue, positions filtered by the multi-target tracker are dashed yellow.

### REFERENCES

- [1] V. Chamola, P. Kotes, A. Agarwal, Naren, N. Gupta, and M. Guizani, "A comprehensive review of unmanned aerial vehicle attacks and neutralization techniques," *Ad Hoc Networks*, vol. 111, p. 102324, 2021. [Online]. Available: <https://www.sciencedirect.com/science/article/pii/S1570870520306788>
- [2] F.-L. Chipier, A. Martian, C. Vladeanu, I. Marghescu, R. Craciunescu, and O. Fratu, "Drone detection and defense systems: Survey and a software-defined radio-based solution," *Sensors*, vol. 22, no. 4, 2022. [Online]. Available: <https://www.mdpi.com/1424-8220/22/4/1453>
- [3] M. Ghasri and M. Maghrebi, "Factors affecting unmanned aerial vehicles' safety: A post-occurrence exploratory data analysis of drones' accidents and incidents in australia," *Safety Science*, vol. 139, p. 105273, 2021. [Online]. Available: <https://www.sciencedirect.com/science/article/pii/S0925753521001181>
- [4] M. Stampa, A. Sutorma, U. Jahn, J. Thiem, C. Wolff, and C. Röhrig, "Maturity levels of public safety applications using unmanned aerial systems: a review," *Journal of Intelligent & Robotic Systems*, vol. 103, no. 1, pp. 1–15, 2021.
- [5] M. Vrba, D. Heřt, and M. Saska, "Onboard marker-less detection and localization of non-cooperating drones for their safe interception by an autonomous aerial system," *RA-L*, vol. 4, no. 4, pp. 3402–3409, Oct 2019.
- [6] M. Vrba and M. Saska, "Marker-less micro aerial vehicle detection and localization using convolutional neural networks," *RA-L*, vol. 5, no. 2, pp. 2459–2466, April 2020.

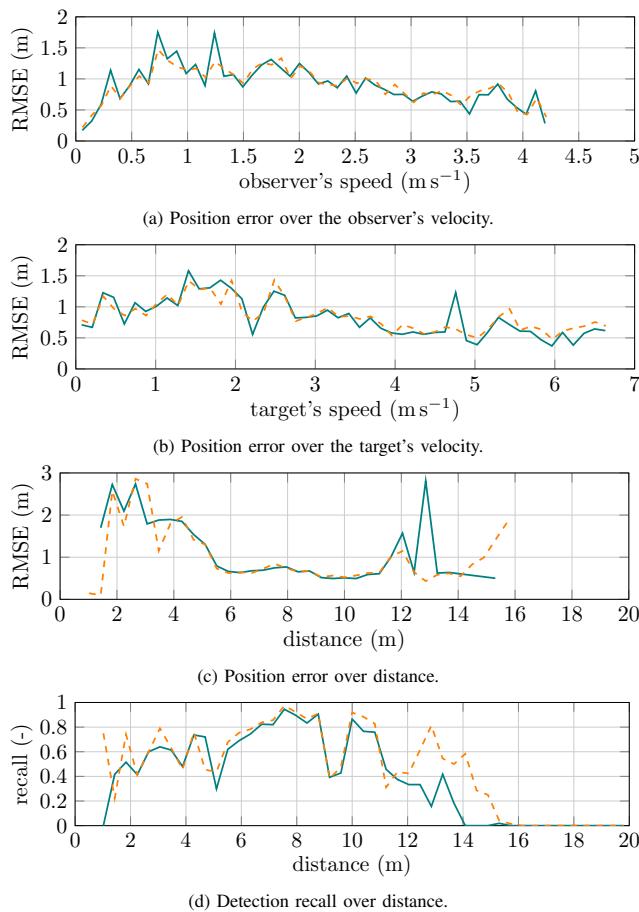


Figure 8: Results from the real-world experiments. Detected positions are in blue, positions filtered by the multi-target tracker are dashed yellow.

- [7] M. García, R. Caballero, F. González, A. Viguria, and A. Ollero, "Autonomous drone with ability to track and capture an aerial target," in *ICUAS*, 2020, pp. 32–40.
- [8] M. Beul, S. Bultmann, A. Rochow, R. A. Rosu, D. Schleich, M. Splitter, and S. Behnke, "Visually guided balloon popping with an autonomous mav at mbzirc 2020," in *SSRR*, 2020, pp. 34–41.
- [9] M. Zhao, T. Anzai, F. Shi, T. Maki, T. Nishio, K. Ito, N. Kuromiya, K. Okada, and M. Inaba, "Versatile multilinked aerial robot with tilted propellers: Design, modeling, control, and state estimation for autonomous flight and manipulation," *Journal of Field Robotics*, vol. 38, no. 7, pp. 933–966, 2021.
- [10] A. Barišić, F. Petric, and S. Bogdan, "Brain over brawn: Using a stereo camera to detect, track, and intercept a faster UAV by reconstructing the intruder's trajectory," *Field Robotics*, vol. 2, no. 1, pp. 222–240, mar 2022.
- [11] M. Vrba, Y. Stasinchuk, T. Báča, V. Spurný, M. Petrlík, D. Heřt, D. Žaitlík, and M. Saska, "Autonomous capture of agile flying objects using UAVs: The MBZIRC 2020 challenge," *Robotics and Autonomous Systems*, vol. 149, p. 103970, March 2022. [Online]. Available: <https://www.sciencedirect.com/science/article/pii/S0921889021002396>
- [12] V. Pritzl, M. Vrba, P. Stepan, and M. Saska, "Cooperative Navigation and Guidance of a Micro-Scale Aerial Vehicle by an Accompanying UAV using 3D LiDAR Relative Localization," in *2022 International Conference on Unmanned Aircraft Systems (ICUAS)*. IEEE, June 2022, pp. 526–535.
- [13] J. Park, S. Park, D. Kim, and S. Park, "Leakage mitigation in heterodyne FMCW radar for small drone detection with stationary point concentration technique," *T-MTT*, vol. 67, no. 3, pp. 1221–1232, 2019.
- [14] A. D. de Quevedo, F. I. Urzaiz, J. G. Menoyo, and A. A. Lopez, "Drone detection with X-band ubiquitous radar," in *IRS*, 2018, pp. 1–10.
- [15] Z. Shi, X. Chang, C. Yang, Z. Wu, and J. Wu, "An acoustic-based surveillance system for amateur drones detection and localization," *TVT*, vol. 69, no. 3, pp. 2731–2739, 2020.
- [16] F. Svanstrom, C. Englund, and F. Alonso-Fernandez, "Real-Time Drone Detection and Tracking With Visible, Thermal and Acoustic Sensors," *arXiv e-prints*, p. arXiv:2007.07396, July 2020.
- [17] M. Hammer, B. Borgmann, M. Hebel, and M. Arens, "UAV detection, tracking, and classification by sensor fusion of a 360° lidar system and an alignable classification sensor," in *Laser Radar Technology and Applications XXIV*, M. D. Turner and G. W. Kamerman, Eds., vol. 11005, International Society for Optics and Photonics. SPIE, 2019, pp. 99 – 108.
- [18] S. Dogru and L. Marques, "Drone detection using sparse lidar measurements," *IEEE Robotics and Automation Letters*, vol. 7, no. 2, pp. 3062–3069, 2022.
- [19] A. Barišić, F. Petric, and S. Bogdan, "Sim2air - synthetic aerial dataset for uav monitoring," *IEEE Robotics and Automation Letters*, vol. 7, no. 2, pp. 3757–3764, 2022.
- [20] A. Schumann, L. Sommer, J. Klatte, T. Schuchert, and J. Beyerer, "Deep cross-domain flying object classification for robust UAV detection," in *AVSS*, Aug 2017, pp. 1–6.
- [21] A. Rozantsev, V. Lepetit, and P. Fua, "Detecting flying objects using a single moving camera," *IEEE Transactions on Pattern Analysis and Machine Intelligence*, vol. 39, no. 5, pp. 879–892, 2017.
- [22] A. Carrio, J. Tordesillas, S. Vemprala, S. Saripalli, P. Campoy, and J. P. How, "Onboard detection and localization of drones using depth maps," *Access*, vol. 8, pp. 30480–30490, 2020.
- [23] M. Petrlík, P. Petracek, V. Kratky, T. Musil, Y. Stasinchuk, M. Vrba, T. Baca, D. Hert, M. Pecka, T. Svoboda, and M. Saska, "Uavs beneath the surface: Cooperative autonomy for subterranean search and rescue in darpa sub7," preprint *arXiv:2206.08185*, 2022, submitted to Field Robotics Special Issue: DARPA Subterranean Challenge.
- [24] J. Zhang and S. Singh, "LOAM: Lidar odometry and mapping in real-time," in *Robotics: Science and Systems*, vol. 2, no. 9, 2014.
- [25] A. Hornung, K. M. Wurm, M. Bennewitz, C. Stachniss, and W. Burgard, "Octomap: An efficient probabilistic 3d mapping framework based on octrees," *Autonomous robots*, vol. 34, no. 3, pp. 189–206, 2013.
- [26] D. Meagher, "Geometric modeling using octree encoding," *Computer graphics and image processing*, vol. 19, no. 2, pp. 129–147, 1982.
- [27] D. Duberg and P. Jensfelt, "Ufomap: An efficient probabilistic 3d mapping framework that embraces the unknown," *IEEE Robotics and Automation Letters*, vol. 5, no. 4, pp. 6411–6418, 2020.
- [28] D. De Gregorio and L. Di Stefano, "Skimap: An efficient mapping framework for robot navigation," in *2017 IEEE International Conference on Robotics and Automation (ICRA)*, 2017, pp. 2569–2576.
- [29] R. B. Rusu and S. Cousins, "3D is here: Point Cloud Library (PCL)," in *IEEE International Conference on Robotics and Automation (ICRA)*, Shanghai, China, May 9-13 2011.
- [30] G. Guennebaud, B. Jacob, *et al.*, "Eigen v3," <http://eigen.tuxfamily.org>, 2010.
- [31] M. Quigley, K. Conley, B. P. Gerkey, J. Faust, T. Foote, J. Leibs, R. Wheeler, and A. Y. Ng, "ROS: an open-source Robot Operating System," in *ICRA Workshop on Open Source Software*, 2009.
- [32] T. Baca, M. Petrlík, M. Vrba, V. Spurný, R. Penicka, D. Hert, and M. Saska, "The mrs uav system: Pushing the frontiers of reproducible research, real-world deployment, and education with autonomous unmanned aerial vehicles," *Journal of Intelligent & Robotic Systems*, vol. 102, no. 26, pp. 1–28, May 2021.
- [33] H. Moravec and A. Elfes, "High resolution maps from wide angle sonar," in *Proceedings. 1985 IEEE International Conference on Robotics and Automation*, vol. 2, 1985, pp. 116–121.
- [34] C. O'Meadhra, W. Tabib, and N. Michael, "Variable resolution occupancy mapping using gaussian mixture models," *IEEE Robotics and Automation Letters*, vol. 4, no. 2, pp. 2015–2022, 2019.
- [35] P. Petracek, V. Kratky, M. Petrlík, T. Baca, R. Kratochvil, and M. Saska, "Large-scale exploration of cave environments by unmanned aerial vehicles," *IEEE Robotics and Automation Letters*, vol. 6, no. 4, pp. 7596–7603, October 2021.
- [36] V. Krátký, P. Petráček, T. Báča, and M. Saska, "An autonomous unmanned aerial vehicle system for fast exploration of large complex indoor environments," *Journal of Field Robotics*, vol. 38, no. 8, pp. 1036–1058, May 2021.
- [37] Y. Xie, Y. Tang, R. Zhou, Y. Guo, and H. Shi, "Map merging with terrain-adaptive density using mobile 3d laser scanner," *Robotics and Autonomous Systems*, vol. 134, p. 103649, 2020.
- [38] R. B. Rusu, "Semantic 3d object maps for everyday manipulation in human living environments," Dissertation, Technische Universität München, München, 2009.
- [39] J. Amanatides, A. Woo, *et al.*, "A fast voxel traversal algorithm for ray tracing," in *Eurographics*, vol. 87, no. 3, 1987, pp. 3–10.

- [40] A. Genz, “Numerical computation of rectangular bivariate and trivariate normal and t probabilities,” *Statistics and Computing*, vol. 14, pp. 251–260, 2004.
- [41] D. Hert, T. Baca, P. Petracek, V. Kratky, V. Spurny, M. Petrlik, M. Vrba, D. Zaitlik, P. Stoudek, V. Walter, P. Stepan, J. Horyna, V. Pritzl, G. Silano, D. Bonilla Licea, P. Stibinger, R. Penicka, T. Nascimento, and M. Saska, “MRS Modular UAV Hardware Platforms for Supporting Research in Real-World Outdoor and Indoor Environments,” in *2022 International Conference on Unmanned Aircraft Systems (ICUAS)*. IEEE, June 2022, pp. 1264–1273.